In Vivo Imaging of Transport and Biocompatibility of Single Silver Nanoparticles in Early Development of Zebrafish Embryos

Kerry J. Lee,[†,§] Prakash D. Nallathamby,[†,§] Lauren M. Browning,[†] Christopher J. Osgood,[‡] and Xiao-Hong Nancy Xu[†,*]

[†]Department of Chemistry and Biochemistry and [‡]Department of Biological Sciences, Old Dominion University, Norfolk, Virginia 23529. [§]These authors contributed equally to this work.

ABSTRACT Real-time study of the transport and biocompatibility of nanomaterials in early embryonic development at single-nanoparticle resolution can offer new knowledge about the delivery and effects of nanomaterials *in vivo* and provide new insights into molecular transport mechanisms in developing embryos. In this study, we directly characterized the transport of single silver nanoparticles into an *in vivo* model system (zebrafish embryos) and investigated their effects on early embryonic development at single-nanoparticle resolution in real time. We designed highly purified and stable (not aggregated and no photodecomposition) nanoparticles and developed single-nanoparticle optics and *in vivo* assays to enable the study. We found that single Ag nanoparticles (5–46 nm) are transported into and out of embryos through chorion pore canals (CPCs) and exhibit Brownian diffusion (not active transport), with the diffusion coefficient inside the chorionic space (3×10^{-9} cm^2/s) ~26 times lower than that in egg water (7.7×10^{-8} cm^2/s). In contrast, nanoparticles were trapped inside CPCs and the inner mass of the embryos, showing restricted diffusion. Individual Ag nanoparticles were observed inside embryos at each developmental stage and in normally developed, deformed, and dead zebrafish, showing that the biocompatibility and toxicity of Ag nanoparticles and types of abnormalities observed in zebrafish are highly dependent on the dose of Ag nanoparticles, with a critical concentration of 0.19 nM. Rates of passive diffusion and accumulation of nanoparticles in embryos are likely responsible for the dose-dependent abnormalities. Unlike other chemicals, single nanoparticles can be directly imaged inside developing embryos at nanometer spatial resolution, offering new opportunities to unravel the related pathways that lead to the abnormalities.

KEYWORDS: biocompatibility · diffusion · embryos · *in vivo* imaging · silver nanoparticle · single-nanoparticle optics · toxicity · transport · zebrafish

Nanomaterials possess unique physical and surface properties, which have inspired plans for a wide spectrum of applications, such as target-specific vehicles for *in vivo* sensing, diagnosis, and therapy (*e.g.*, nanomedicine and drug delivery).[1–5] These unique properties may also incite toxicity, damaging *in vivo* systems of interest and posing risks to human health and the environment.[6] Thus, we select an effective *in vivo* model system (zebrafish embryos) and one type of nanomaterials (Ag nanoparticles) and focus on probing the transport mechanism and dose-dependent biocompatibility of the nanomaterials *in vivo,* targeting the initial entry step of nanomaterials into embryos, and aiming to demonstrate their potential applications and address their potential adverse effects. Real-time study of the transport and biocompatibility of single nanoparticles in the early development of embryos will provide new insights into molecular transport mechanisms and the structure of developing embryos at nanometer spatial resolution *in vivo,* as well as assessing the biocompatibility of single-nanoparticle probes *in vivo*.

Currently, fluorescent probes, such as fluorescent dyes and proteins, are commonly used for *in vivo* imaging. Unfortunately, fluorescence probes suffer photodecomposition, limiting the time available for probing dynamic events of interest. Currently, nanoparticle probes such as semiconductor quantum dots (QDs) and noble metal nanoparticles are becoming popular and powerful probes for living cellular and *in vivo* imaging.[7–12] QDs have unique optical properties in comparison with fluorescence dyes and proteins, such as a tunable narrow emission spectrum, broad excitation spectrum, high photostability, and long fluorescence lifetime.[8,9,13] Nevertheless, QDs still suffer a certain degree of photodecomposition, and it remains a challenge to prevent aggregation of intracellular QDs.

Noble metal nanoparticles (Ag, Au, and their alloys) have unique optical properties, such as surface plasmon resonance (SPR), showing the dependence of optical properties on the size and shape of the

*Address correspondence to xhxu@odu.edu.

Received for review May 30, 2007 and accepted September 4, 2007.

Published online September 28, 2007.
10.1021/nn700048y CCC: $37.00

nanoparticles, surrounding environment, and dielectric constant of the embedding medium.[14–17] Recent research has demonstrated the feasibility of using the intrinsic optical properties of the nanoparticles for imaging single living cells in real time with sub-100 nm spatial resolution and millisecond time resolution.[10–12] Among noble metal nanoparticles, Ag nanoparticles offer the highest quantum yield (QY) of Rayleigh scattering. For example, the QY of Rayleigh scattering of 2 nm Ag nanoparticles is about 10^4 times higher than that of a single fluorescent dye molecule (*e.g.*, Rhodamine 6G). The scattering intensity of noble metal nanoparticles is proportional to the volume of nanoparticles.[14–17] Thus, Ag nanoparticles are extremely bright and can be directly observed using dark-field single-nanoparticle optical microscopy and spectroscopy (SNOMS). Unlike fluorescent probes and QDs, these noble metal nanoparticles do not suffer photodecomposition and can be used as probes to continuously monitor dynamic events for an extended period of time. Furthermore, the localized surface plasmon resonance (LSPR) spectra (color) of nanoparticles show size dependence.[14–16] Thus, one can use the color (LSPR spectra) index of these multicolor nanoparticles as a nanometer-size index (CASI) to directly measure membrane transport of nanoparticles and changes in the size of membrane pores at the nanometer scale in real time. [10–12]

Nevertheless, like other nanoparticle probes (*e.g.*, QDs), the biocompatibility of Ag nanoparticles awaits further and systematic study.[6,12] Thus, it is important to develop *in vivo* model systems to effectively screen biocompatibility of nanoparticle probes in real time while exploring the potential of nanoparticles for *in vivo* imaging.

Zebrafish (*Danio rerio*) have unique advantageous features over other vertebrate model systems (*e.g.*, mouse, rat, human).[18–22] For example, the early embryonic development of zebrafish is completed rapidly, within 120 h, with well-characterized developmental stages. The embryos are transparent and develop outside of their mothers, permitting direct visual detection of pathological embryonic death and maldevelopment phenotypes as well as study of real-time transport and effects of nanoparticles *in vivo*. Therefore, zebrafish embryos offer a unique opportunity to investigate the effects of nanoparticles on intact cellular systems that communicate with each other to orchestrate the events of early embryonic development. Genetic screens of zebrafish phenotypes indicate similarities to human diseases, and protein sequences of drug-binding sites in zebrafish and humans show a high degree of identities.[18,22] Thus, zebrafish have served as a vital model system for screening drug targets for curing human diseases. Large numbers of embryos can be generated rapidly at low cost, which can serve as an ideal *in vivo* assay for screening biocompatibility, pharmacological efficacy, and toxicity of nanoparticle probes. Fish are renowned for their ability to bioconcentrate trace contaminants in the environment. Human consumption of fish suggests a direct impact on human health by potential release of nanomaterials into the environment.

Although the zebrafish has been a popular model for screening chemical toxicity[19] and drugs,[22] it has not yet been reported for screening the biocompatibity, therapeutic effects, and toxicity of nanoparticles. Furthermore, in all reported nanotoxicity studies, conventional toxicological assays were used primarily, which cannot characterize the dose of nanoparticles *in vivo* and in real time. Typically, nanoparticles were injected into *in vivo* systems,[6,23] which is highly invasive. Many of these studies used unpurified nanoparticles or functionalized nanoparticles and did not consider effects of residual chemicals produced during nanoparticle synthesis persisting in nanoparticle solutions, leading to inconclusive results.[6]

Currently, the biocompatibility of nanoparticles used as labeling agents for imaging of cells and organisms quite often is not well-characterized. The primary challenges of using nanoparticle probes for *in vivo* imaging and probing the effects of nanoparticles on living cells and organisms are (i) to maintain the stability (prevent aggregation and photodecomposition) of nanoparticles in physiological medium and *in vivo,* (ii) to develop real-time imaging tools for tracking the diffusion and location of individual nanoparticles *in vivo*, and (iii) to invent powerful means to characterize individual nanoparticles *in vivo* and in real time. In this study, we have accomplished all of these objectives, achieving a major advance in the study of single nanoparticles *in vivo*.

RESULTS AND DISCUSSION

Synthesis and Characterization of Ag Nanoparticles. We synthesized spherical Ag nanoparticles with average diameter of 11.6 ± 3.5 nm by reducing $AgClO_4$ with reducing agents (sodium citrate and sodium borohydride) using well-tuned synthesis conditions as described in Methods. We then carefully washed the nanoparticles to remove trace chemicals remaining from their synthesis using centrifugation, generating highly purified nanoparticles. We characterized the stability, size, and optical properties of these purified Ag nanoparticles incubated in egg water (1.2 mM NaCl) for 120 h using UV–vis absorption spectroscopy, SNOMS, dynamic light scattering (DLS), and high-resolution transmission electron microscopy (HR-TEM) (Figure 1).

The absorption spectra of freshly prepared and washed nanoparticles before and after incubation with egg water for 120 h (Figure 1A, a and b) show an absorbance of 0.736 at a peak wavelength of 396–400 nm, indicating that Ag nanoparticles are very stable (not aggregated) in egg water (1.2 mM NaCl). We determined

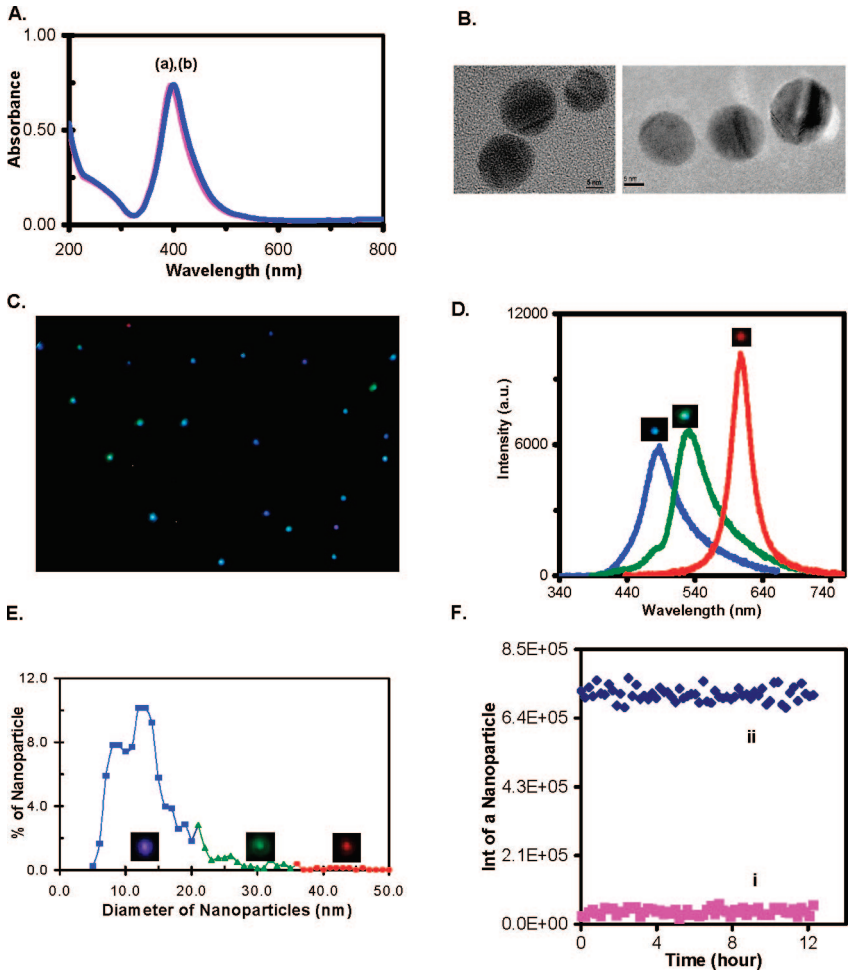

Figure 1. Characterization of optical properties and stability of Ag nanoparticles. (A) Representative UV–vis absorption spectra of 0.71 nM Ag nanoparticles well-dispersed in egg water at 28 °C for (a) 0 and (b) 120 h, showing that the peak absorbance and wavelength at 396 nm remain unchanged for 120 h. (B) Representative HR-TEM images of Ag nanoparticles, showing the size and spherical shape of single Ag nanoparticles. Scale bar = 5 nm. (C) Representative dark-field optical image of single Ag nanoparticles, showing that the majority of nanoparticles are blue, with some being green and a few red. (D) Representative LSPR spectra (color) of single Ag nanoparticles, exhibiting peak wavelengths at 452 (blue), 531 (green), and 601 nm (red). (E) Histogram of the size and color distribution of individual Ag nanoparticles, showing the average size of nanoparticles to be 11.6 ± 3.5 nm, with 74% 5–15 nm (blue), 23% 16–30 nm (green), and 1% 31–46 nm (red). (F) Representative plots of scattering intensity of (i) a representative single nanoparticle and (ii) background *versus* illumination time, showing that single Ag nanoparticles resist photobleaching and blinking.

the effect of salt concentration (the positive control experiment) by increasing NaCl concentration and found that nanoparticles are stable in the presence of NaCl up to 10 mM but begin to aggregate in 100 mM NaCl, showing a red shift of peak absorbance wavelength (~2–3 nm) and a decrease in absorbance. The size of nanoparticles, measured by DLS, increased from 10.1 ± 2.0 to 24.4 ± 2.7 nm in the presence of 100 mM NaCl. The presence of a sufficiently high concentration of NaCl (100 mM) appears to reduce the thickness of the electric double-layer on the surface of nanoparticles and decrease the zeta-potential below its critical point, leading to aggregation of nanoparticles.

We characterized the size of Ag nanoparticles using HR-TEM and DLS before and after incubation with egg water for 120 h, showing that the size of the nanoparticles remained unchanged, with an average diameter of 11.6 ± 3.5 nm.

Furthermore, we characterized the optical properties of individual nanoparticles using SNOMS (Figure 1C–F). A representative optical image of single nanoparticles in Figure 1C illustrates that the majority of nanoparticles are blue, with some being green and a few red. The representative LSPR spectra of single blue, green, and red nanoparticles show peak wavelengths at 488, 532, and 607 nm (Figure 1D), respectively. The correlation of the color distribution of individual nanoparticles with their size, measured by HR-TEM, shows that the majority (74%) of single nanoparticles, with diameters of 5–15 nm, are blue, 23% of single nanoparticles, with diameters of 16–30 nm, are green, and a very small fraction (1%) of nanoparticles, with diameters of 31–46 nm, are red (Figure 1E). Thus, the color index of single nanoparticles can be used as a size index to directly distinguish and determine the size of nanoparticles (5–46 nm) using SNOMS, even though the size of nanoparticles cannot be measured directly due to the optical diffraction limit. We also found that the distribution of color and size of nanoparticles remained unchanged as nanoparticles were incubated in egg water for 120 h, suggesting that nanoparticles are stable (not aggregated) in egg water at single nanoparticle resolution.

To determine the photostability of Ag nanoparticles, we acquired sequence images of single Ag nanoparticles while those nanoparticles were constantly radiated under a dark-field microscope illuminator (100 W halogen) for 12 h. The illumination power at the sample stage (focal plane of dark-field) was 0.070 ± 0.001 W. Representative plots of scattering intensity of single nanoparticles and background (in the absence of nano-

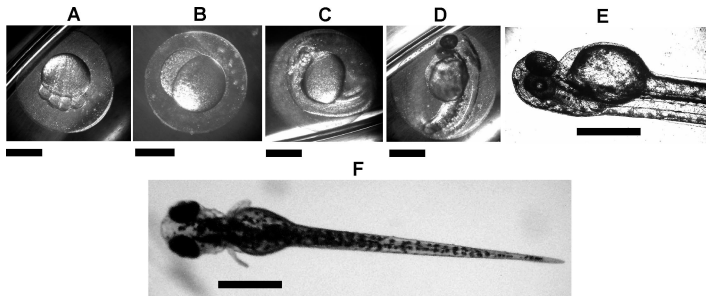

Figure 2. Optical images of the representative developmental stages of a normally developing zebrafish in egg water (in the absence of nanoparticles): (A) 1.25–1.50 hpf (8-cell-stage embryo); (B) 2–2.25 hpf (64-cell-stage embryo); (C) 24 hpf (segmentation-stage embryo); (D) 48 hpf (hatching-stage embryo); (E) 72 hpf (pharyngula-stage embryo); and (F) a completely developed zebrafish at 120 hpf. Scale bar = 500 μm. hpf = hours post-fertilization.

particles) *versus* illumination time in Figure 1F indicate that the scattering intensity of individual single nanoparticles remains unchanged over 12 h, showing that single Ag nanoparticles resist photodecomposition and blinking. Note that the small fluctuations of intensity of single nanoparticles (Figure 1F, i) are similar to those observed from the background (Figure 1F, ii), suggesting that the intensity fluctuations are attributable to the illuminator and the noise level of the CCD camera.

Probing Diffusion and Transport of Single Nanoparticles in Cleavage-Stage Embryos. Representative developmental stages of the zebrafish embryos in the 120 hours post-fertilization (hpf) in Figure 2 are the cleavage-stage embryo (8–64-cell stage), segmentation-stage embryo, hatching-stage embryo, pharyngula-stage embryo, and fully developed zebrafish in the absence of nanoparticles. At the cleavage stage (8–64-cell stage; 0.75–2.25 hpf) (Figure 2A,B), embryos undergo dramatic changes (*e.g.*, rapid cellular division and distinct fate establishment) to lay the foundation for developing the different parts of organs, and a variety of interesting but not yet well-understood biochemical and biophysical events (*e.g.*, cell migration signaling and embryonic pattern formation) occur. This stage is crucial in development, as the foundation and organization of the embryo are being assembled.[24,25] Thus, it is important to understand the diffusion and transport mechanisms among the various parts of the embryo at this particular stage. Cleavage-stage embryos may also be most sensitive to foreign substances,[26] offering an ultrasensitive *in vivo* model system to study the biocompatibility and subtle effects of nanoparticles on the embryonic development.

To study the diffusion and transport of single nanoparticles into cleavage-stage embryos, we incubated Ag nanoparticles with the embryos and directly observed and characterized their transport, showing that Ag nanoparticles (blue, green, and red) transport into the chorionic space (cs) *via* chorion pore canals (CPCs) and enter into the inner mass of the embryo (ime) (Figure 3 and movies 1 and 2, Supporting Information). We used our optical imaging system to directly mea-

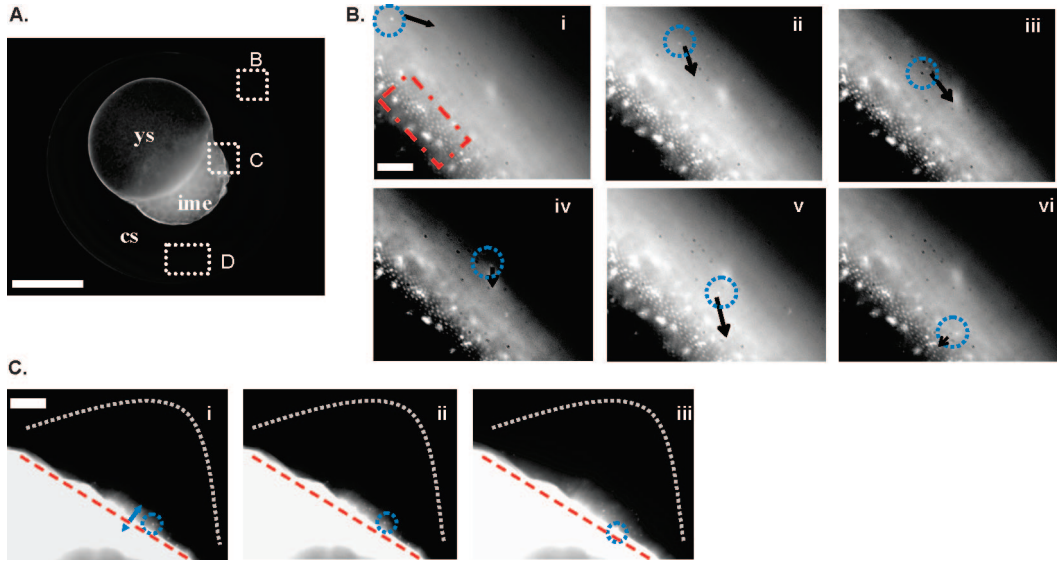

Figure 3. Real-time monitoring and characterization of transport of individual Ag nanoparticles in a cleavage-stage living embryo (64-cell stage; 2–2.25 hpf). (A) Optical image of a cleavage-stage embryo, showing chorionic space (cs), yolk sac (ys), and inner mass of the embryo (ime). The transport of single Ag nanoparticles at the interface of egg water with chorionic space, interface of chorionic space with inner mass of the embryo, and inside chorionic space, as marked by B, C, and D, are shown in movies 1–3 in the Supporting Information, respectively. Snapshots of transport of single nanoparticles at the interfaces of egg water/chorionic space and chorionic space/inner mass of the embryo are illustrated in (B) and (C). LSPR spectra (color) of individual nanoparticles were used to distinguish them from tissue debris or vesicles in embryos. (B) Sequential dark-field optical images, illustrating the transport of single Ag nanoparticles, as indicated by the circle, from the egg water (extra-embryo) into the chorionic space *via* an array of chorion pore canals (CPCs), highlighted by a rectangle. (C) Sequential dark-field optical images, illustrating the transport of single Ag nanoparticles, as indicated by the circle, from chorionic space into inner mass of the embryo. The straight and curved dashed lines illustrate the interfaces of inner mass of the embryo with chorionic space and of chorionic space with egg water, respectively. The time interval between sequential images in (B) and (C) is 25 s. Scale bar = 400 μm (A) and 15 μm (B,C).

sure the chorion pore canals, showing them to be approximately 0.5–0.7 μm in diameter, with distances between the centers of two nearby chorion pore canals of ~1.5–2.5 μm, which agrees well with those measured using TEM.[27] To our knowledge, this study demonstrates the first direct observation of chorion pore canals of single living embryos using optical microscopy. We show that the chorion pore canals are larger than the nanoparticles, permitting the passive diffusion of individual nanoparticles into the chorionic space of embryos.

To determine the transport mechanism of Ag nanoparticles, we utilized the concept of two-dimensional mean square displacement (MSD) and diffusion models (*e.g.*, directed, simple, and stationary Brownian diffusion)[28,29] to investigate each diffusion trajectory of single nanoparticles in egg water, entry into embryos, and inside embryos. To follow the diffusion of single nanoparticles inside various parts of embryos in real time, we used real-time square displacement (RTSD) (diffusion distance at a given time interval), instead of the average (mean) of square displacement over time, because the diffusion coefficient could vary as single nanoparticles diffuse in embryos. This approach allowed us to probe the diffusion of single nanoparticles and the viscosity of the different parts of embryonic fluids (*e.g.*, chorionic space, inner mass of the embryo) in real time. The diffusion coefficient (D) of single nanoparticles in simple Brownian motion is calculated by dividing the slope of a linear plot of RTSD *versus* time by 4 (Note: RTSD $= 4D\Delta t$) (Figure 4B).

Representative diffusion trajectories of single Ag nanoparticles trapped inside chorion pore canals, in chorionic space, and near the inner mass of the embryo, and analysis of these diffusion trajectories using the RTSD method, are shown in Figure 4. The results illustrate that single Ag nanoparticles inside the chorionic space (near either the chorion layers or the inner mass of the embryo) exhibit simple Brownian diffusion (not active transport) with diffusion rate (3×10^{-9} cm^2/s) ~26 times slower than that in egg water (7.7×10^{-8} cm^2/s), showing that single Ag nanoparticles diffuse into the chorionic space *via* passive diffusion and that the viscosity of chorionic space is about 26 times higher than that of egg water.

As nanoparticles make several attempts to enter the chorion layers and inner mass of the embryo, their diffusion patterns are restricted (Figure 4B, a-i, steps in a-ii and a-iii), suggesting that the nanoparticles dock into the chorion pore canals, which halts their normal diffusion. By tracking the entry of individual nanoparticles into chorion pore canals, we measured the period of time that individual nanoparticles stay in the pores, which ranged from 0.1 to 15 s.

We characterized the diffusion coefficient of blue, green, and red nanoparticles in egg water (Figure 4B, b) to determine the possible variation of diffusion coefficients due to the different sizes (radii) of single nanoparticles, showing simple Brownian diffusion with $D = 8.4 \times 10^{-8}$, 6.0×10^{-8}, and 5.5×10^{-8} cm^2/s, respectively. The diffusion coefficients are inversely proportional to the radius of the single nanoparticles, as described by the

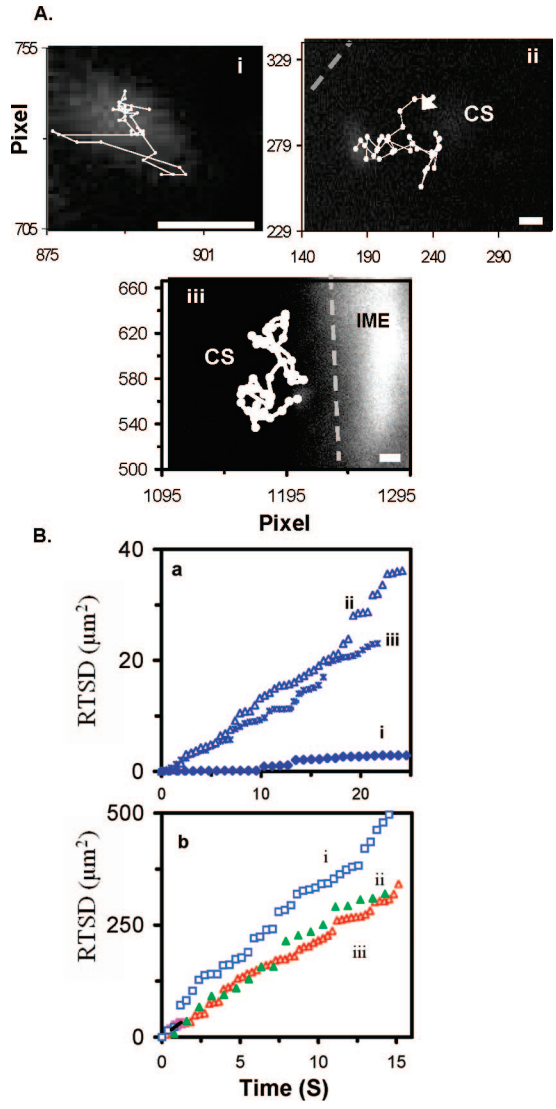

Figure 4. Characterization of transport and diffusion of single Ag nanoparticles in a cleavage-stage (64-cell) living embryo. (A) Diffusion trajectories of single Ag nanoparticles: (i) a red nanoparticle inside the chorion layers, (ii) a blue nanoparticle inside chorionic space, and (iii) a green nanoparticle at the interface of inner mass of the embryo and chorionic space. Their real-time videos are shown in movies 3 and 4 in the Supporting Information. (B) Plots of real-time square displacement (RTSD) as a function of time: (a) Single nanoparticles from the diffusion trajectories shown in (A), illustrating (i) a red nanoparticle in a restricted and stationary diffusion mode with a diffusion coefficient (D) < 1.9×10^{-11} cm^2/s, due to entrapment inside chorion pore canals; (ii) a blue nanoparticle in chorionic space away from the inner mass of the embryo and (iii) a green nanoparticle inside chorionic space near the surface of inner mass of the embryo, both in a simple Brownian motion with $D = 3.4 \times 10^{-9}$ and 2.6×10^{-9} cm^2/s, respectively. (b) Representative single (i) blue, (ii) green, and (iii) red nanoparticles in egg water. All show simple Brownian diffusion with $D = 8.4 \times 10^{-8}$, 6.0×10^{-8}, and 5.5×10^{-8} cm^2/s, respectively.

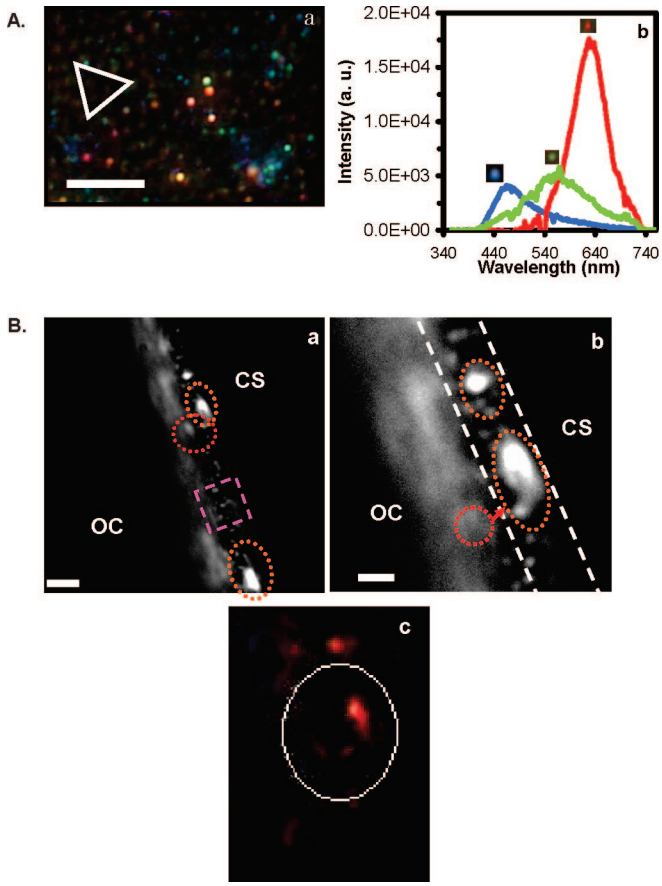

Figure 5. Characterization of Ag nanoparticles embedded in embryos using dark-field SNOMS. (A) Representative (a) color image and (b) LSPR spectra of single Ag nanoparticles embedded in chorion layers, showing that single Ag nanoparticles with multiple colors (blue, green, red) are present inside chorion layers, and some nanoparticles are overlapped with the chorion pore canals (note an array of chorion pore canals, highlighted by a triangle). Scale bar = 1 μm. (B) Representative images of individual Ag nanoparticles embedded in the chorion layers, illustrating those Ag nanoparticles (as indicated by a circle) trapped in the chorion pore canals, outlined by ellipses. The CCD image in (a) is enlarged in (b). A zoom-in of the color image in (b) is shown in (c), indicating that the dark-red nanoparticles clog the chorion pore canals. Scale bar = 10 μm (a) and 2 μm (b). OC = outside chorion.

Stokes–Einstein equation, $D = kT/(6\pi\eta a)$, showing that the diffusion coefficient (D) depends on the viscosity (η) of the medium and the radius (a) of the solute (nanoparticle).[30,31] The diffusion coefficients of the given color (radius) nanoparticles in embryos were studied and compared with those in egg water, showing that the various diffusion coefficients observed in three different parts of embryos (Figure 4B, a) were indeed attributable to the viscosity gradient inside the embryos, but not the different radii of individual nanoparticles.

Characterization of Transport and Embedded Nanoparticles. Images of the transport of single nanoparticles into the chorionic space were recorded using dark-field SNOMS equipped with a color camera, instead of a CCD, showing that nanoparticles of multiple colors transport into the chorionic space (Figure 5A). Note that single Ag nanoparticles exhibit colors (LSPR), which depend on the size and shape of the nanoparticle and the surrounding environment.[14–17] This feature allowed us to distinguish single Ag nanoparticles from any possible tissue debris or vesicle-like particles in embryos, which do not exhibit surface plasmon and hence appear white under dark-field microscopy. We found that the majority of nanoparticles transported into the chorionic space, and some of them overlapped with chorion pore canals (Figure 5A, a). The representative LSPR spectra (colors) of individual nanoparticles inside the chorionic space (Figure 5A, b) show peak wavelengths similar to those observed in egg water (Figure 1D). The results indicate that the majority of nanoparticles remained non-aggregated inside the embryos. Otherwise, we would have observed a significant red shift in the LSPR spectra of individual nanoparticles.

Although the majority of single nanoparticles can freely diffuse into embryos and remain non-aggregated, some single nanoparticles stay in chorion pore canals for an extended period of time. These trapped nanoparticles serve as nucleation sites and aggregate with incoming nanoparticles to form larger particles (dark-red nanoparticles, Figure 5B), clogging chorion pore canals and affecting the embryo's transport. Note that embryos at this developmental stage are free of pigmentation.

As the cleavage-stage (8-cell) embryos chronically treated with lower concentrations of Ag nanoparticles (<0.08 nM) completed their embryonic development at 120 hpf, we characterized Ag nanoparticles embedded in fully developed zebrafish using SNOMS and found that these Ag nanoparticles embedded in multiple organs (retina, brain, heart, gill arches, and tail) of normally developed zebrafish (Figure 6), demonstrating that Ag nanoparticles are biocompatible with embryos at lower concentrations (<0.08 nM). The LSPR spectra of these embedded nanoparticles are similar to those shown in Figure 5A, b. We also performed blank control experiments by imaging 120-hpf zebrafish that developed in the absence of nanoparticles and did not observe the signature LSPR spectra (color) of Ag nanoparticles in these fully developed zebrafish.

Dose-Dependent Biocompatibility and Toxicity. To determine the effect of different doses of Ag nanoparticles on embryonic development, we treated the cleavage-stage (8-cell) embryos chronically with various concentrations of Ag nanoparticles (0–0.71 nM) and carefully monitored and characterized the vital developmental stages (24, 48, 72, 96, and 120 hpf). The results in Figures 7 and 8 show that biocompatibility of Ag nanoparticles and the types of abnormalities in treated zebrafish are both highly dependent on the dose of Ag nanoparticles. In the presence of lower concentrations (<0.08 nM) of nanoparticles, the percentage of normally developed zebrafish observed is higher than that of dead and deformed zebrafish. Note that both normal and deformed zebrafish developed from the cleavage-stage (8-cell) embryos that had been simulta-

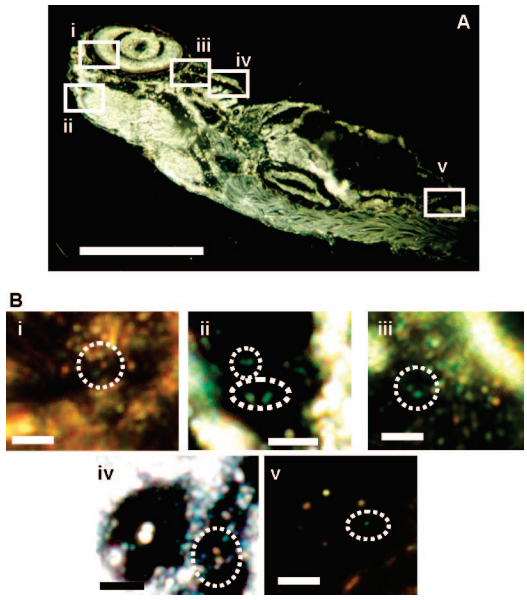

Figure 6. Characterization of individual Ag nanoparticles embedded inside a fully developed (120 hpf) zebrafish using dark-field SNOMS. (A) Optical image of a fixed, normally developed zebrafish. The rectangles highlight representative areas: (i) retina, (ii) brain (mesencephalon cavity), (iii) heart, (iv) gill arches, and (v) tail. (B) Zoom-in optical images of single Ag nanoparticles embedded in those tissue sections outlined in (A). Dashed circles outline the representative embedded individual Ag nanoparticles. Scale bar = 400 μm (A) and 4 μm (B).

neously incubated with the same nanoparticle solution. Thus, the results suggest that some embryos might be more tolerant to the nanoparticles than others. The results also suggest that Ag nanoparticles might affect the development of embryos stochastically due to the random diffusion of nanoparticles.

As nanoparticle concentration increases, the number of normally developed zebrafish decreases, while the number of dead zebrafish increases (Figure 7A). As nanoparticle concentration increases beyond 0.19 nM, only dead and deformed zebrafish are observed, showing a critical concentration of Ag nanoparticles in the development of zebrafish embryos (Figure 7). The blank (negative) control experiments, conducted by replacing nanoparticles with the supernatant resulting from washing Ag nanoparticles, show that the survival rate of zebrafish is independent of the dose of supernatant (Figure 7B), demonstrating that residual chemicals from nanoparticle synthesis are not responsible for the deformation and death of zebrafish, but rather the nanoparticles that were used to treat the zebrafish embryos (Figure 7A).

The number of deformed zebrafish increased to its maximum as nanoparticle concentration increased to 0.19 nM, and then decreased as nanoparticle concentration increased from 0.19 to 0.71 nM (Figure 7C) because the number of dead zebrafish increased. Interestingly, the types of viable deformities exhibit a high dependence on the nanoparticle concentration (Figure

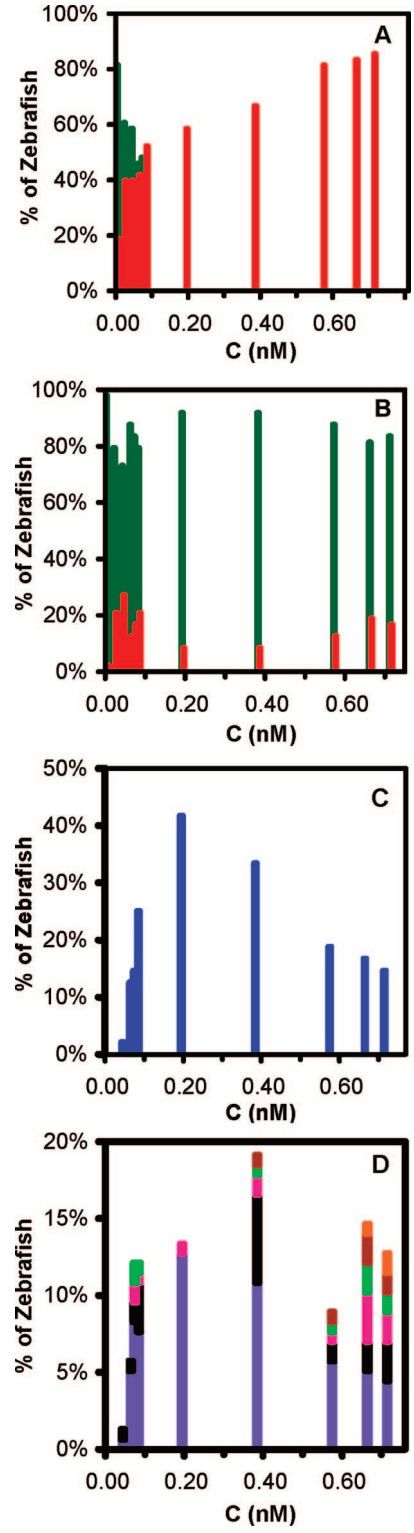

Figure 7. Histograms of distribution of normally developed (green) and dead (red) zebrafish, (A) *versus* concentration of Ag nanoparticles and (B) *versus* concentration of supernatants resulting from washing Ag nanoparticles (negative control). (C) Histogram of distribution of deformed zebrafish (120 hpf) *versus* concentration of Ag nanoparticles. (D) Histogram of distribution of five representative types of deformities of the zebrafish *versus* concentration of Ag nanoparticles: finfold abnormality (purple), tail and spinal cord flexure and truncation (black), cardiac malformation (pink), yolk sac edema (light green), head edema (brown), and eye abnormality (orange).

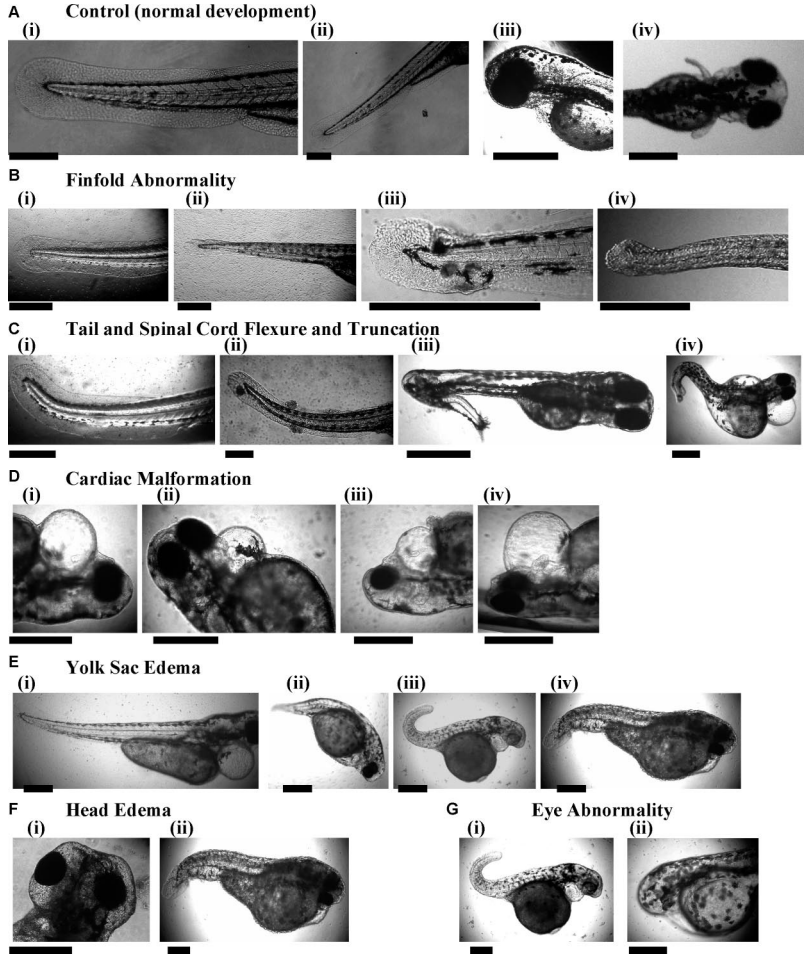

Figure 8. Representative optical images of (A) normally developed and (B–G) deformed zebrafish. (A) Normal development of (i) finfold, (ii) tail/spinal cord, (iii) cardiac, (iii,iv) yolk sac, cardiac, head, and eye. (B–G) Deformed zebrafish: (B) finfold abnormality; (C) tail and spinal cord flexure and truncation; (D) cardiac malformation; (E) yolk sac edema; (F) head edema, showing both (i) head edema and (ii) head edema and eye abnormality; (G) eye abnormality, showing both (i) eye abnormality and (ii) eyeless. Scale bar = 500 μm. More zebrafish deformations observed in these experiments are summarized in Table I of the Supporting Information.

7D). For example, finfold abnormality and tail/spinal cord flexure and truncation were observed in zebrafish treated with all tested nanoparticle concentrations (0.04–0.71 nM), with the highest occurrences at 0.19 and 0.38 nM, respectively. Cardiac malformation and yolk sac edema were observed in zebrafish treated with slightly higher nanoparticle concentrations (0.07–0.71 nM), with the highest occurrences at 0.66 nM. In contrast, head edema and eye deformity were observed only with the higher concentrations of nanoparticles, 0.44–0.71 and 0.66–0.71 nM, respectively. Among all types of observed deformities, finfold abnormality occurred at the highest rate, followed by tail and spinal cord flexure and truncation, and then cardiac malformation and yolk sac edema, and finally head edema and eye abnormality, which were rarely observed deformations of zebrafish and quickly led to zebrafish death.

Representative zebrafish deformations induced by nanoparticles are illustrated in Figure 8B–G and summarized in the Supporting Information. In comparison with the normally developed zebrafish shown in Figure 8A, we found characteristics of finfold abnormality (Figure 8B), tail and spinal cord flexure and truncation (Figure 8C), cardiac malformation (Figure 8D), yolk sac edema (Figure 8E), head edema (Figure 8F), and eye abnormality (Figure 8G) in zebrafish that developed from the 8-cell embryos treated chronically by Ag nanoparticles. Interestingly, multiple deformities could occur in a single zebrafish at the higher nanoparticle concentrations (>0.38 nM). For example, in yolk sac edema zebrafish, we also observed tail/spinal cord flexure, finfold abnormality, and cardiac malformation (Figure 8C-iv and E-ii), head edema (Figure 8E-ii, E-iv, and F-ii), and eye abnormality (Figure 8G-i). These findings suggest that specific embryonic developmental pathways might be co-regulated and that some deformities (*e.g.*, finfold, tail, spinal cord) are much more sensitive to the nanoparticles than others (*e.g.*, head edema, eye abnormality).

To determine possible targets for further genomic and proteomic studies and evaluate the toxicity of Ag nanoparticles against well-studied toxic chemicals, such as cadmium, dichloroacetic acid (DCA), 2,3,7,8-tetrachlorodibenzo-*p*-dioxin (TCDD), and ethanol, we compared the characteristics of deformation of zebrafish induced by Ag nanoparticles with those generated by well-known toxic chemicals. We found that the observed finfold abnormality and tail/spinal cord flexure and truncation induced by Ag nanoparticles (Figure 8B,C) are similar to those observed in zebrafish treated with DCA and cadmium,[32,33] indicating possible common targets of malformation during development. The observed cardiac malformation and yolk sac edema in this study (Figure 8D,E) are also similar to those observed in zebrafish treated with DCA and cadmium.[32,33] The shrunken ventricular myocardium observed in cardiac malformed zebrafish induced by nanoparticles (Figure 8D) is similar to the observation in zebrafish treated with TCDD.[34] Head edema and eye abnormality (Figure 8F,G-i) have also been found to result in zebrafish treated with cadmium.[32]

Although eye malformation (a cycloptic eye development) had been observed in zebrafish treated with ethanol,[35] the deformation was different from what we observed (eyeless, no formation of retina or lens, Figure 8G-ii). Thus, the eyeless deformation (Figure 8G-ii), an undeveloped set of optic cups with no retina or eye lens, is, to our knowledge, a new occurrence of malformation that has not been reported previously. This ab-

normality may be related to the nanoparticles disrupting the regulators or signaling cascades involved with the normal development of the neural retinal layers and the lens of the zebrafish's eye. A transcription factor, Pax-6, has been studied and shown to affect the development of the eye retinal layers. In Pax-6 mutants, the lens fails to develop.[35,36] However, another transcription factor, Six-6, regulating neural retinal development in zebrafish has not been studied in detail, and it may also play a role in eye deformation.[36] Further studies are needed to determine whether Ag nanoparticles inhibit or regulate the expression of transcription factors (*e.g.*, Pax-6 and Six-6), leading to the eyeless deformation.

Plausible explanations for the high dependence of embryonic abnormalities on the dose of nanoparticles include the following: (i) The rate of passive diffusion (permeability) and accumulation of nanoparticles in chorion pore canals and embryos highly depends on the concentration gradient of nanoparticles. Thus, the dose of nanoparticles plays a vital role in determining the rate and amount of nanoparticles that can penetrate into particular compartments of embryos, and the rate and number of chorion pore canals blocked by the aggregation of nanoparticles (Figures 3–5). (ii) The accumulated nanoparticles inside embryos can also alter the charge, diffusion, and interactions of biomolecules (*e.g.*, nucleic acids, proteins such as transcription factors, signaling molecules) in a dose-dependent manner, leading to interference or malfunctioning of signaling cascades.

Taken together, these results suggest that specific pathways of embryonic development respond to Ag nanoparticles in a dose-dependent manner, demonstrating that the nanoparticles may elicit unique responses from embryonic neural development pathways. The study demonstrates the possibility of fine-tuning the dose of nanoparticles to (i) selectively target specific pathways to create particular phenotypes, (ii) selectively generate specific mutations in zebrafish, and (iii) serve as potential therapeutic agents to treat specific disorders in embryonic development. Unlike other chemicals, single nanoparticles can be traced and imaged inside developing embryos and developed zebrafish with nanometer spatial resolution in real time, offering new opportunities to unravel the related pathways that lead to the abnormalities. Work is in progress to identify the related specific pathways and signaling cascades at the genomic and proteomic levels and to further explore potential therapeutic effects of nanoparticles.

SUMMARY

In summary, we have designed, synthesized, and characterized single-nanoparticle optical probes (individual Ag nanoparticles) for studying their transport, biocompatibility, and toxicity in early development of zebrafish embryos in real time. We have shown that single Ag nanoparticles resist photodecomposition and blinking and can be directly monitored in embryos for an extended period of time. Furthermore, individual Ag nanoparticles exhibit size-dependent LSPR spectrum (color), which permits us (i) to distinguish them from tissue debris and vesicles in embryos, (ii) to directly image and characterize the sizes of individual nanoparticles in solution and in living embryos in real time, (iii) to probe their diffusion, transport mechanism, and biocompatibility in living embryos in real time, and (iv) to investigate the embryonic fluids (*e.g.*, viscosity) at nanometer spatial resolution in real time. We found that individual Ag nanoparticles can passively diffuse into developing embryos *via* chorion pore canals, create specific effects on embryonic development, and selectively generate particular phenotypes in a dose-dependent manner. The early embryos are highly sensitive to the nanoparticles, showing the possibility of using zebrafish embryos as an *in vivo* assay to screen the biocompatibility and toxicity of nanomaterials. This study represents the first direct observation of passive diffusion of nanoparticles into an *in vivo* system (an important aquatic species), suggesting that the release of large amounts of Ag nanoparticles into aquatic ecosystems (*e.g.*, rivers) may have drastic environmental consequences, should the sizes of nanomaterials remain unchanged during environmental transport. This study also represents the first rigorous study and characterization of nanotoxicity and nanobiocompatibility ever performed by investigating the effect of highly purified nanoparticles *in vivo* in real time and considering the effect of possible trace chemicals from nanoparticle synthesis.

METHODS

Synthesis and Characterization of Silver Nanoparticles. Silver nanoparticles were synthesized by reducing a 0.1 mM silver perchlorate solution with a freshly prepared ice-cold solution of 3 mM sodium citrate and 10 mM sodium borohydride under stirring overnight; the solution was then filtered through a 0.22 μm filter.[11,37] The nanoparticles were washed twice with nanopure water using centrifugation to remove the chemicals involved in nanoparticle synthesis, and the nanoparticle pellets were resuspended in nanopure water before incubation with embryos. The washed Ag nanoparticles are very stable (non-aggregated) in nanopure water for months and remain stable in egg water throughout the entire experiments (120 hpf). The supernatants of nanoparticle solutions after the second washing were collected for control experiments to study the effect of trace chemicals involved in nanoparticle synthesis on the development of embryos. The concentration, optical properties, and size of nanoparticles were characterized using UV–vis spectroscopy, dark-field single-nanoparticle optical microscopy and spectroscopy (SNOMS),[10–12] high-resolution transmission electron microscopy (HR-TEM, FEI Tecnai G2 F30 FEG), and dynamic light scattering (DLS, Nicomp 380ZLS particle sizing system). Our dark-field SNOMS has been well described previously for real-time imaging and spectroscopic characterization of single nanoparticles in single living cells and for single molecule detection.[10–12,31,38,39] An electron-multiplying charge-coupled device (EMCCD) or LN

back-illuminated CCD camera coupled with a SpectraPro-150 (Roper Scientific) was used in this study. All chemicals were purchased from Sigma and used without further purification or treatment.

To determine the photostability of single Ag nanoparticles, we acquired sequence images of single Ag nanoparticles using an EMCCD camera with exposure time at 100 ms and readout time of 40.6 ms while these nanoparticles were constantly radiated under dark-field microscope illumination (100 W halogen) for 12 h. The illumination power at the sample stage (focal plane of dark field) was 0.070 ± 0.001 W. The integrated scattering intensity of single nanoparticles and background (in the absence of nanoparticles) within a 20 × 20 CCD pixel area was measured. The integrated scattering intensity of background is subtracted from that of the same size detection area in the presence of individual nanoparticles to calculate the scattering intensity of single nanoparticles. The experiments were repeated at least three times. The average subtracted integrated intensity of the single nanoparticles and background was plotted as a function of time (Figure 1F). The fluctuations of intensity of single nanoparticles were compared with those of background to determine the photostability (photodecomposition and blinking) of single nanoparticles.

Breeding and Monitoring of Zebrafish Embryos. Wild-type adult zebrafish (Aquatic Ecosystems) were maintained, bred, and collected as described previously.[40] Embryos were collected and transferred into a Petri dish containing egg water (1.2 mM stock salts in deionized (DI) water), washed twice with egg water to remove the surrounding debris, and placed into 24-well plates, with each well containing two embryos in egg water. Each developmental stage of the embryos in the wells was directly imaged by bright-field optical microscopy using an inverted microscope equipped with a 4× objective and a digital camera.

***In Vivo* Characterization and Analysis of Transport and Dose-Dependent Biocompatibility and Toxicity of Nanoparticles.** Cleavage-stage living embryos (8–64-cell stage; 0.75–2.25 hpf) that had been incubated with 0.19 nM nanoparticles for a given time (0–2 h) were either immediately imaged to investigate the transport of nanoparticles into embryos or carefully rinsed with DI water to remove external nanoparticles, and then placed in a home-made microwell containing DI water to image the diffusion and transport of nanoparticles inside the embryos in real time using our SNOMS.

To study the dose-dependent effects of nanoparticles on embryonic development, a dilution series of washed Ag nanoparticle solutions (0, 0.04, 0.06, 0.07, 0.08, 0.19, 0.38, 0.57, 0.66, and 0.71 nM) was incubated chronically with cleavage-stage (8-cell) embryos in egg water for 120 hpf. Each experiment was carried out at least three times, and a total of 35–40 embryos were studied for each concentration to gain representative statistics. Nanoparticle concentrations were calculated as described previously.[41] Embryos in egg water in the absence of nanoparticles and in the presence of supernatant were placed in two rows of the 24-well plates as control experiments of untreated embryos and for probing the effect of possible trace chemicals from nanoparticle synthesis, respectively. The embryos in the 24-well plates were incubated at 28.5 °C and directly observed at room temperature using an inverted microscope equipped with a digital camera at 24, 48, 72, 96, and 120 hpf.

Characterization of Nanoparticles Embedded inside Embryos and Fully Developed Zebrafish. To characterize the embedded nanoparticles in the tissues of treated zebrafish, we selected living developed zebrafish that had been chronically incubated with a given concentration (0.04 nM) of nanoparticles for 120 hpf since their cleavage (8-cell) stage and carefully rinsed the zebrafish with DI water to remove external nanoparticles. The fixed zebrafish were prepared using 10% buffered formalin *via* a standard histology protocol of tissue sample preparation.[42] Thin-layer microsections (~5 μm thickness) of tissue samples were prepared by carefully dissecting the tissues of interest (*e.g.*, eye retina, brain, heart, gill arch, tail, and spinal cord) under microscopy using a microtome. The embedded nanoparticles in the tissues were directly characterized using SNOMS (Figure 6).

Acknowledgment. We thank E. Dupont for her helpful assistance in literature search and CharFac of University of Minnesota (a NNIN site funded by NSF) for their assistance in characterizing Ag nanoparticles using HRTEM. This work is supported in part by NSF (NIRT BES 0507036) and NIH (R01 GM076440). K.J.L., P.D.N., L.M.B., and E. Dupont are grateful for support from NSF-GRAS (BES 0541661), Dominion Scholar Fellowship, NIH-GRAS (R01 GM076440-01S1), and NSF-RETS (BES 0542448), respectively.

Supporting Information Available: Table I, summarizing representative and rare deformities of zebrafish treated chronically with given Ag nanoparticle concentrations (0.04–0.71 nM) for 120 hpf since the cleavage (8-cell) stage, showing the high dependence of severities of deformation on nanoparticle concentration. Four real-time videos: movies 1 and 2, illustrating the direct observation of single Ag nanoparticles entering into chorionic space of a cleavage-stage (64-cell) embryo (2–2.25 hpf) from egg water *via* an array of chorion pore canals and transporting into the inner mass of the embryos, respectively, and movies 3 and 4, showing the diffusion trajectories of single nanoparticles in a cleavage-stage (64-cell) embryo, near or in chorion pore canals of chorion layers, and in chorion pore (either near the chorion layer or near the surface of the inner mass of the embryos), respectively. This information is available free of charge *via* the Internet at http://pubs.acs.org.

REFERENCES AND NOTES

1. Tiwari, S. B.; Amiji, M. M. A Review of Nanocarrier-Based CNS Delivery Systems. *Curr. Drug Delivery* **2006**, *3* (2), 219–232.
2. Xu, X. H. N.; Patel, R. P. Nanoparticles for Live Cell Dynamics. In *Encyclopedia of Nanoscience and Nanotechnology*; Nalwa, H. S., Ed.; American Scientific Publishers: Stevenson Ranch, CA, 2004; Vol. 7, pp 189–192.
3. Xu, X. H. N.; Patel, R. P. Imaging and Assembly of Nanoparticles in Biological Systems. In *Handbook of Nanostructured Biomaterials and Their Applications in Nanobiotechnology*; Nalwa, H. S., Ed.; American Scientific Publishers: Stevenson Ranch, CA, 2005; Vol. 1, pp 435–456.
4. Xu, X. H. N.; Song, Y.; Nallathamby, P. D. Probing Membrane Transport of Single Live Cells Using Single Molecule Detection and Single Nanoparticle Assay. In *New Frontiers in Ultrasensitive Bioanalysis: Advanced Analytical Chemistry Applications in Nanobiotechnology, Single Molecule Detection, and Single Cell Analysis*; Xu, X. H. N., Ed.; Wiley: Hoboken, NJ, 2007; pp 41–65.
5. Yamada, T.; Iwasaki, Y.; Tada, H.; Iwabuki, H.; Chuak, M. K. I.; VandenDriessche, T.; Fukuda, H.; Kondo, A.; Ueda, M.; Seno, M.; Tanizawa, K.; Kuroda, S. Nanoparticles for the Delivery of Genes and Drugs to Human Hepatocytes. *Nat. Biotechnol.* **2003**, *21*, 885–890.
6. Nel, A.; Xia, T.; Madler, L.; Li, N. Toxic Potential of Materials at the Nanolevel. *Science* **2006**, *311*, 622–627.
7. Agrawal, A.; Zhang, C.; Byassee, T.; Tripp, R. A.; Nie, S. Counting Single Native Biomolecules and Intact Viruses with Color-Coded Nanoparticles. *Anal. Chem.* **2006**, *78*, 1061–1070.
8. Bruchez, M., Jr.; Moronne, M.; Gin, P.; Weiss, S.; Alivisatos, A. P. Semiconductor Nanocrystals as Fluorescent Biological Labels. *Science* **1998**, *281*, 2013–2016.
9. Chan, W. C.; Nie, S. Quantum Dot Bioconjugates for Ultrasensitive Nonisotopic Detection. *Science* **1998**, *281*, 2016–2018.
10. Kyriacou, S.; Brownlow, W.; Xu, X.-H. N. Nanoparticle Optics for Direct Observation of Functions of Antimicrobial Agents in Single Live Bacterial Cells. *Biochemistry* **2004**, *43*, 140–147.
11. Xu, X. H. N.; Brownlow, W. J.; Kyriacou, S. V.; Wan, Q.; Viola, J. J. Real-Time Probing of Membrane Transport in Living Microbial Cells Using Single Nanoparticle Optics and Living Cell Imaging. *Biochemistry* **2004**, *43*, 10400–10413.
12. Xu, X. H. N.; Chen, J.; Jeffers, R. B.; Kyriacou, S. V. Direct Measurement of Sizes and Dynamics of Single Living

Membrane Transporters Using Nano-Optics. *Nano Lett.* **2002**, *2*, 175–182.
13. Alivisatos, A. P. Perspectives on the Physical Chemistry of Semiconductor Nanocrystals. *J. Phys. Chem. B* **1996**, *100*, 13226–13239.
14. Bohren, C. F.; Huffman, D. R. *Absorption and Scattering of Light by Small Particles*; Wiley: New York, 1983; pp 287–380.
15. Kreibig, U.; Vollme, M. *Optical Properties of Metal Clusters*; Springer: Berlin, 1995; pp 14–123.
16. Mie, G. Beiträg Zur Optik Trüber Medien, Speziell Kolloidaler Metrallosungen. *Ann. Phys.* **1908**, *25*, 377–445.
17. Mulvaney, P. Surface Plasmon Spectroscopy of Nanosized Metal Particles. *Langmuir* **1996**, *12*, 788–800.
18. den Hertog, J. Chemical Genetics: Drug Screens in Zebrafish. *Biosci. Rep.* **2005**, *25*, 289–297.
19. Hill, A. J.; Teraoka, H.; Heideman, W.; Peterson, R. E. Zebrafish as a Model Vertebrate for Investigating Chemical Toxicity. *Toxicol. Sci.* **2005**, *86* (1), 6–19.
20. Kahn, P. Zebrafish Hit the Big Time. *Science* **1994**, *264*, 904–905.
21. Teraoka, H.; Dong, W.; Hiraga, T. Zebrafish as a Novel Experimental Model for Developmental Toxicology. *Congenital Anomalies* **2003**, *43*, 123–132.
22. Zon, L. I.; Peterson, R. T. In Vivo Drug Discovery in the Zebrafish. *Nat. Rev. Drug Discovery* **2005**, *4*, 35–44.
23. Rieger, S.; Kulkarni, R. P.; Darcy, D.; Fraser, S. E.; Koster, R. W. Quantum Dots Are Powerful Multipurpose Vital Labeling Agents in Zebrafish Embryos. *Dev. Dyn.* **2005**, *234*, 670–681.
24. Luckenbill-Edds, L. Introduction: Research News in Developmental Biology in 1895 and 1995. *Am. Zool.* **1997**, *37*, 213–219.
25. Strehlow, D.; Heinrich, G.; Gilbert, W. The Fates of the Blastomeres of the 16-Cell Zebrafish Embryo. *Development* **1994**, *120*, 1791–1798.
26. Hoar, W. S.; Randall, D. J. *Fish Physiology: The Physiology of Developing Fish, Part A, Eggs and Larvae*; Academic Press: New York, 1988; pp 253–255.
27. Rawson, D. M.; Zhang, T.; Kalicharanv, D.; Jongebloed, W. L. Field Emission Scanning Electron Microscopy and Transmission Electron Microscopy Studies of the Chorion, Plasma Membrane and Syncytial Layers of the Gastrula Stage Embryo of the Zebrafish Brachydanio Rerio: A Consideration of the Structural and Functional Relationships with Respect to Cryoprotectant Penetration. *Aquacult. Res.* **2000**, *31*, 325–336.
28. Kusumi, A.; Sako, Y. Compartmental Structure of the Plasma Membrane for Receptor Movements as Revealed by a Nanometer-Level Motion Analysis. *J. Cell. Biol.* **1994**, *125*, 1251–1264.
29. Kusumi, A.; Sako, Y.; Yamamoto, M. Confined Lateral Diffusion of Membrane Receptors as Studied by Single Particle Tracking (Nanovid Microscopy). Effects of Calcium-Induced Differentiation in Cultured Epithelial Cells. *Biophys. J.* **1993**, *65*, 2021–2040.
30. Tinoco, I.; Sauer, K.; Wang, J.; Puglisi, J. D. Molecular Motion and Transport Properties. In *Physical Chemistry—Principles and Applications in Biological Sciences*; Prentice Hall: Englewood Cliffs, NJ, 2002; pp 274–290.
31. Xu, X. H. N.; Jeffers, R. B.; Gao, J.; Logan, B. Novel Solution-Phase Immunoassays for Molecular Analysis of Tumor Markers. *Analyst* **2001**, *126*, 1285–1292.
32. Hallare, A. V.; Schirlinga, M.; Luckenbacha, T.; Kohler, H.-R.; Triebskorn, R. Combined Effects of Temperature and Cadmium on Developmental Parameters and Biomarker Responses in Zebrafish (Danio Rerio) Embryos. *J. Therm. Biol.* **2005**, *30*, 7–17.
33. Williams, F. E.; Sickelbaugh, T. J.; Hassoun, E. Modulation by Ellagic Acid of DCA-Induced Developmental Toxicity in the Zebrafish (*Danio Rerio*). *J. Biochem. Mol. Toxicol.* **2006**, *20*, 183–190.
34. Antkiewicz, D. S.; Burns, C. G.; Carney, S. A.; Peterson, R. E.; Heideman, W. Heart Malformation Is an Early Response to TCDD in Embryonic Zebrafish. *Toxicol. Sci.* **2005**, *84*, 368–377.
35. Arenzana, F. J.; Carvan, M. J., III; Aijon, J.; Sanchez-Gonzalez, R.; Arevalo, R.; Porteros, A. Teratogenic Effects of Ethanol Exposure on Zebrafish Visual System Development. *Neurotoxicol. Teratol.* **2006**, *28*, 342–348.
36. Jean, D.; Ewan, K.; Gruss, P. Molecular Regulators Involved in Vertebrate Eye Development. *Mech. Dev.* **1998**, *76*, 3–18.
37. Lee, P. C.; Meisel, D. Adsorption and Surface-Enhanced Raman of Dyes on Silver and Gold Sols. *J. Phys. Chem. B* **1982**, *86*, 3391–3395.
38. Kyriacou, S. V.; Nowak, M. E.; Brownlow, W. J.; Xu, X. H. N. Single Live Cell Imaging for Real-Time Monitoring of Resistance Mechanism in *Pseudomonas Aeruginosa*. *J. Biomed. Opt.* **2002**, *7*, 576–586.
39. Xu, X. H. N.; Brownlow, W. J.; Huang, S.; Chen, J. Real-Time Measurements of Single Membrane Pump Efficiency of Single Living Pseudomonas Aeruginosa Cells Using Fluorescence Microscopy and Spectroscopy. *Biochem. Biophys. Res. Commun.* **2003**, *305*, 79–86.
40. Westerfield, M. *The zebrafish book: A Guide for the Laboratory Use of Zebrafish (Danio Rerio*)*; University of Oregon Press: Eugene, OR, 1993 (http://zfin.org/zf_info/zfbook/zfbk.html).
41. Xu, X.-H. N.; Huang, S.; Brownlow, W.; Salatia, K.; Jeffers, R. Size and Temperature Dependence of Surface Plasmon Absorption of Gold Nanoparticles Induced by Tris(2,2′-bipyridine)ruthenium(II). *J. Phys. Chem. B* **2004**, *108*, 15543–15551.
42. Mohideen, M.-A. P. K.; Beckwith, L. G.; Tsao-Wu, G. S.; Moore, J. L.; Wong, A. C. C.; Chinoy, M. R.; Cheng, K. C. Histology-Based Screen for Zebrafish Mutants with Abnormal Cell Differentiation. *Dev. Dyn.* **2003**, *228*, 414–423.